# Analog System for Computing Health Indicators in Bearing Fault Diagnosis using Piezoelectric Cantilevers

P. Peralta-Braz[a], E. Atroshchenko[b], S.P.A. Bordas[a]

[a]*Department of Engineering, University of Luxembourg, Luxembourg*
[b]*School of Civil and Environmental Engineering, University of New South Wales, Sydney, Australia*

**Abstract**

This paper proposes a novel analog computing framework for bearing fault diagnosis using piezoelectric energy harvesters (PEHs). The system leverages the harvest vibrational energy to compute health indicators (HIs) directly in the analog domain, thereby reducing the need for high-frequency data acquisition and digital post-processing. A numerical model based on isogeometric analysis is employed to describe the electromechanical behavior of the PEH, while the Intelligent Maintenance Systems (IMS) dataset is used for validation. Results show that the energy accumulated in a capacitor by the PEH can serve as a reliable HI, enabling the identification of critical degradation milestones such as the early fault point, elbow point, and remaining useful life (RUL). Compared with conventional approaches, the proposed method achieves savings in sensing energy and wireless transmission, paving the way for self-powered, ultra-low-power smart bearing.

*Keywords:* Piezoelectric Energy Harvester, Bearing Fault Diagnosis, Vibration Monitoring, Predictive Maintenance, Condition Monitoring, Industrial Wireless Monitoring, Smart Machinery.

## 1. Introduction

Bearings are essential components in today's industries. They are designed to minimise friction in rotating shafts, maintain alignment, and support loads, making them indispensable in sectors such as transportation, manufacturing, and energy production, among others [1]. However, their exposure to severe operating conditions makes them particularly prone to failure, contributing to 45-55% of mechanical breakdowns [2]. This has significant economic consequences, with the manufacturing industry estimated to lose approximately one billion dollars annually [3]. Among different bearing types, rolling bearings (illustrated in Figure 1*a*) are widely used due to their efficiency and mechanical simplicity. These components consist of three main elements: the outer ring, the inner ring, and a set of rolling elements (balls) that reduce friction and allow smooth rotation between the rings. Faults may arise in any of these components, producing distinct patterns that facilitate diagnostic analysis. Consequently, the development of data-driven approaches has garnered considerable attention as an effective solution for addressing bearing deterioration in large-scale industrial processes [4]. These approaches infer the bearing's condition by analysing data obtained from operational machinery [5]. Among the most commonly used data sources are vibration signals [6, 1], due to their high sensitivity, which enables the identification of the degradation process.

The degradation process in bearings has been well described in the literature. It can be divided into three distinct stages based on the behaviour of a Health Indicator (HI), as represented in Figure 1*b*. In Stage I, the bearing operates under normal conditions with no evident signs of damage, and the HI remains nearly constant. As the system transitions into Stage II, an early fault point is

reached, indicating the initiation of minor defects. Although these defects have a moderate impact on performance, the HI begins to increase gradually and linearly. In Stage III, beginning at the so-called elbow point, the bearing experiences accelerated degradation, as reflected by a sharp rise in the HI. This stage is associated with the rapid propagation of damage leading to functional failure. It is important to note that the duration of each stage can vary significantly between bearings due to differences in manufacturing, operating conditions, and the inherent randomness of fault propagation.

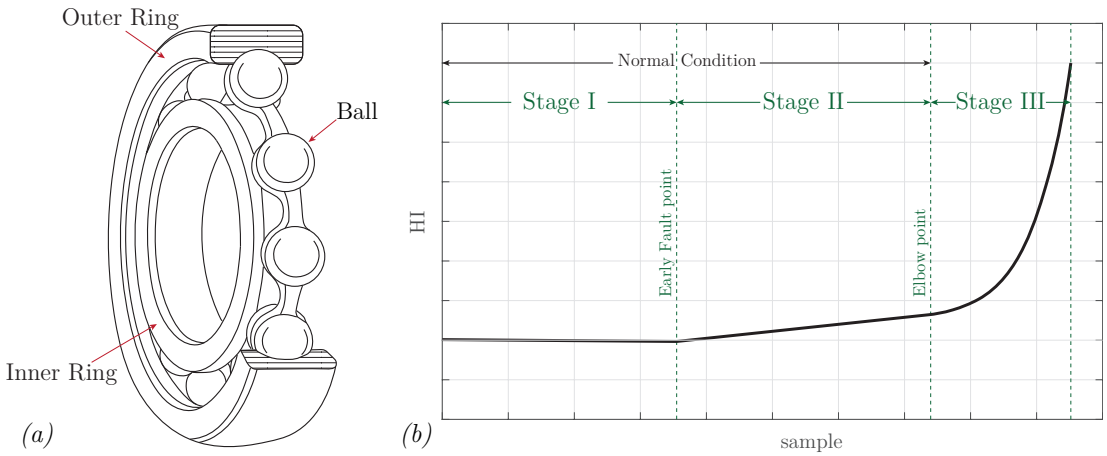


Figure 1: ($a$) Schematic representation of a rolling bearing, composed of the outer ring, inner ring, and rolling elements (balls). ($b$) Typical degradation trajectory of a bearing based on a HI, illustrating three stages: Stage I (good condition), Stage II (slow degradation), and Stage III (accelerated degradation).

Therefore, the Health Index (HI) is essential for describing bearing deterioration, providing the foundation for early fault identification and condition assessment. In recent years, numerous efforts have been directed on proposed HI construction approaches. Traditional methods rely on feature extraction through signal processing techniques [7] in the time, frequency, and time-frequency domains. Statistical indicators in the time domain, including Variance [8], Root Mean Square (RMS) [9, 10], and higher-order moments such as Kurtosis and Skewness [11, 12], have been explored as effective HIs within particular diagnostic frameworks. Moreover, techniques such as the Fourier and Wavelet transforms [13], Singular Value Decomposition (SVD) [14], and Empirical Mode Decomposition (EMD) [15] have been utilized to facilitate the analysis of signals within both the frequency and time–frequency domains. Also, HI derivates by the construction from multiple diagnostic techniques into a single, interpretable fault indicator, frameworks based on fuzzy inference system [16], Mahalanobis Distance and Cumulative Sum (MD-CUMSUM) [17], Adaptive Weighted Signal Preprocessing Technique (AWSPT) [18] have been proposed. Another important theory used to estimate a HI is the Information entropy [19, 20, 21].

In addition, Deep Learning (DL) methods have also been employed for constructing HIs across different domains. Convolutional Neural Networks (CNNs) have been widely explored to extract discriminative features from the time domain [22, 23, 24, 25, 26, 27], and time–frequency domain representations [28, 29, 30, 31]. Recurrent Neural Networks (RNNs) have also been proposed for modeling temporal dependencies in the degradation process and generating HI trajectories [32]. More recently, there has been a growing trend toward developing unsupervised strategies for HI construction. For instance, hybrid architectures such as convolutional autoencoders [33] and sparse autoencoder-based deep neural networks have been used for fault detection in multi-component systems [34]. Furthermore, probabilistic approaches based on Gaussian Mixture Models (GMMs) have been proposed to approximate the probability density function of the signal, enabling the computation of effective HIs.

These include metrics based on divergence measures such as the Kullback–Leibler divergence (KLD) [35], Jensen–Rényi divergence[36], and Wasserstein distance [35, 37].

Overall, HIs presented in the literature have demonstrated high reliability for bearing-related prognostic tasks. In this sense, future research should focus on integrating health index (HI) estimation with low-power, cost-effective hardware solutions that can be seamlessly integrated into machinery components [38]. In this context. the concept of smart bearings [39] has garnered increasing research interest and has become a prominent topic in the field. Unlike conventional bearings, these systems incorporate IoT technologies to transmit key operational parameters to remote monitoring platforms, typically cloud-based servers, thereby enabling online condition monitoring and early fault detection [40, 41]. Companies such as Schaeffler Group, Fersa and SKF have contributed to the development of this technology [42]. One of the main challenges lies in enabling smart bearings to operate autonomously over extended periods [41, 43]. These efforts have driven the integration of energy harvesting (EH) and energy storage technologies, both of which have seen significant advancements in recent years, enabling the development of self-powered IoT devices—such as smart bearings [44]. As discussed above, vibration is an excellent source of information for inferring Health Indicators (HIs). However, the use of vibrational energy harvesting technologies remains challenging, as the generated output power is typically on the order of tens of microwatts [45], generally insufficient to provide a robust, continuous power supply or to achieve full energy autonomy on its own.

As illustrated in Figure 2*a*, in a conventional smart bearing condition monitoring system [40, 41, 43], the process begins with **signal acquisition**, where a sensor captures analog mechanical waves from the environment, typically at sampling frequencies in the kilohertz range, and forwards the data to a processor for digitisation. The resulting high volume of digital data is then transmitted via a transceiver to a cloud server. In the data processing stage, the signal undergoes several preprocessing steps such as noise filtering, detrending, normalisation, and transformations including FFT and wavelet analysis. Next, in the **feature extraction** phase, relevant health indicators such as RMS, kurtosis, spectral energy, and envelope indicators are computed to characterise the system's condition. This step significantly reduces the volume of data by extracting only the most meaningful features. Finally, in the **fault recognition** stage, evaluation algorithms such as machine learning models, threshold comparisons, or pattern classification techniques are applied to detect and diagnose faults.

The primary objective in the design of self-powered smart bearings is to achieve energy-neutral operation (ENO) [46], which refers to maintaining a balance between power generation and consumption. Achieving this goal requires minimizing power consumption wherever possible. The selection of system components plays a critical role in this regard. For instance, typical accelerometers consume power in the milliwatt range [41]. Likewise, the choice of transceiver technology is crucial and largely depends on the volume of data to be transmitted, which in machine condition monitoring typically lies in the tens of kilohertz range [47, 41]. In addition to efforts aimed at reducing energy consumption during wireless transmission [48], duty cycling techniques have also been explored [49]. However, these strategies do not specifically address the energy bottleneck introduced by high-frequency sampling. In particular, during the **signal acquisition** stage, overall energy consumption is approximately proportional to the sampling frequency [50].

A promising approach to address the high-frequency sampling bottleneck is edge computing [51]. The core idea is to preprocess and analyse data at the edge of the network, closer to the data source, rather than sending it to a cloud server. By doing so, this approach enables efficient handling of critical information while managing less essential data locally, thereby minimising the volume of data that needs to be transmitted. Analysing the conventional smart bearing condition monitoring paradigm

presented in Figure 2*a*, a critical step can be identified in the feature extraction stage, where the high volume of sampled data is significantly reduced to a few HIs used for fault recognition. Therefore, implementing the concept of edge computing to compute the HI before digitization could have a major impact on energy consumption. In this sense, the use of piezoelectric energy harvesters (PEHs) for simultaneous energy harvesting and sensing has shown promising performance in various scenarios [52], as they can convert mechanical vibrations into usable electrical power while also extracting valuable information to infer the system's state. This opens the possibility of designing a PEH-based analog system [53] capable of computing a health indicator directly at the edge, without relying on an external power source. Once the HI is computed, it can be passed through the A/D converter, enabling simplified and efficient processing while minimising the energy costs associated with the wireless transmission of high-frequency signals. This new approach for smart bearing is represented in Figure 2*b*.

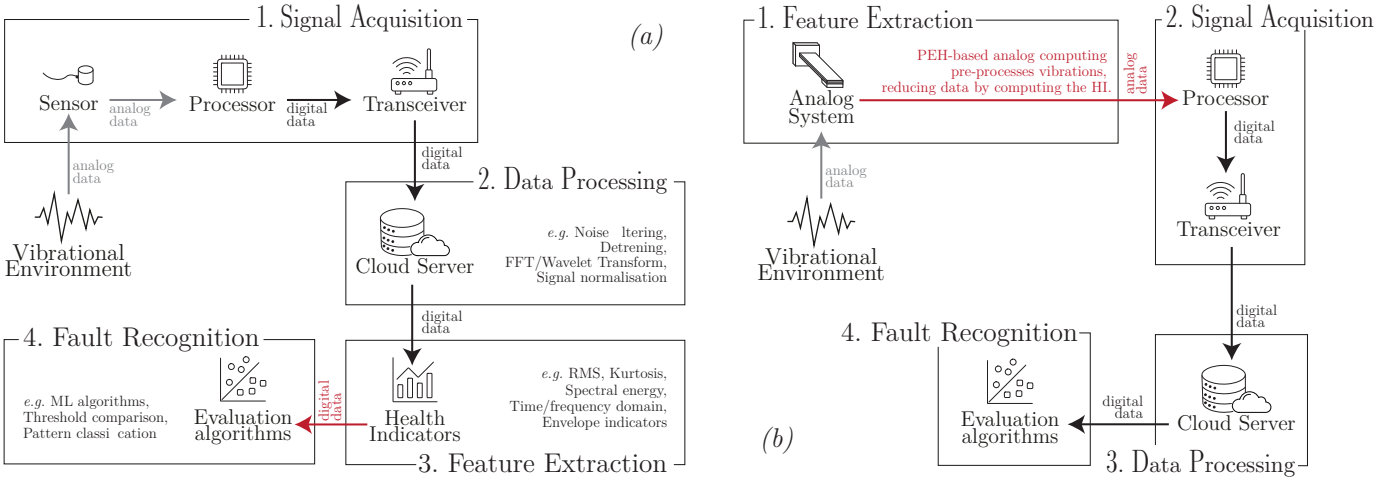


Figure 2: Comparison between (*a*) the conventional paradigm for bearing monitoring and (*b*) the proposed approach incorporating an analog computing system. In red, the stages where data reduction occurs are highlighted. The proposed system performs analog-domain feature extraction prior to digitisation.

This work proposes an integrated degradation monitoring framework that combines energy-efficient hardware design with analog computation of a health indicator (HI) using a PEH-based system, enabling condition inference of the bearing while substantially reducing power consumption. The study evaluates a PEH-based analog system, using a numerical model [54] to describe its behaviour and testing it on the publicly available Intelligent Maintenance Systems (IMS) dataset [7]. The use of a public dataset is motivated by the objective of establishing a benchmark scenario that is widely recognized within the research community. This choice not only enhances comparability with prior studies but also ensures standardized and robust validation of the results. The proposed framework is designed for online degradation monitoring.

The contributions of this paper can be summarised as follows:

- Propose a novel analog computing framework for bearing degradation monitoring that significantly reduces the volume of collected data, thereby lowering energy consumption associated with digitization and wireless transmission.

- Demonstrate, for the first time, that the energy accumulated in a capacitor by a PEH can serve as a reliable feature for computing a HI capable of identifying key degradation milestones.

- Quantify the energy savings of the proposed system compared to conventional approaches.

The remainder of the paper is organised as follows. Section 2 presents the PEH-based numerical framework used to estimate the HI for describing bearing degradation. Section 3 describes the IMS public dataset employed to validate the proposed approach. Section 4 presents an implementation of the framework to demonstrate its ability to identify key degradation milestones, including the early fault point, elbow point, and RUL. Section 5 quantifies the advantages of the framework in terms of energy consumption savings. Finally, Section 6 provides concluding remarks.

## 2. Modeling of the Electromechanical Analog System for Health Indicator Computation

The aim of this section is to present the proposed fault diagnosis system, specifically designed for low-power operation with minimal structural intervention. The system is compact and intended to be seamlessly integrated into the bearing housing (see Figure $3a$). A central component of the system is a PEH, which converts the bearing's vibrations into electrical energy and enables condition monitoring through analog signal process. To accurately characterise its behaviour, a numerical model of the PEH is employed, and its details are presented in this section. Additionally, the accompanying analog electrical circuit used to compute the HI, which quantifies the bearing's degradation, is also introduced.

The model used to describe the dynamic behaviour of the PEH is based on the Kirchhoff–Love plate theory and Hamilton's principle for coupled electromechanical systems. It is solved numerically using the IsoGeometric Analysis (IGA) framework. The formulation presented in [54] has demonstrated high accuracy with a reasonable computational cost. Figure $1b-c$ illustrates the PEH, which consists of a substructure layer with thickness $h_s$ and two piezoelectric layers, each with thickness $h_p$. All layers are rectangular and share the same width $W$ and length $L$. The device is mounted on the vibration source (in this case, the bearing housing) and connected to the electrical circuit responsible for computing the HI. In particular, IGA utilizes B-Splines $N_I$ to parameterize the device's domain and approximate the relative deflection of the mid-plane using a vector of control variables $\mathbf{w} \in \mathbb{R}^{N\times 1}$, where $N$ denotes the total number of degrees of freedom. Consequently, this approach leads to a coupled system of differential equations, represented as,

$$\mathbf{M}\ddot{\mathbf{w}} + \mathbf{C}\dot{\mathbf{w}} + \mathbf{K}\mathbf{w} - \mathbf{\Theta}v(t) = \mathbf{F}a_b(t) \tag{1}$$

$$C_p\dot{v}(t) + \mathbf{\Theta}^T\dot{\mathbf{w}} = -i(t) \tag{2}$$

Here, equation (1) represents the mechanical equation of motion with electrical coupling, while equation (2) denotes the electrical circuit equation with mechanical coupling. The matrix $\mathbf{M} \in \mathbb{R}^{N\times N}$ is the mass matrix, $\mathbf{K} \in \mathbb{R}^{N\times N}$ is the stiffness matrix, and $\mathbf{C} \in \mathbb{R}^{N\times N}$ is the mechanical damping matrix. The vector $\mathbf{F} \in \mathbb{R}^{N\times 1}$ represents the mechanical forces, while $\mathbf{\Theta} \in \mathbb{R}^{N\times 1}$ is the electromechanical coupling vector. $C_p$ denotes the piezoelectric capacitance, $i$ is the electrical current in the piezoelectric system, $a_b(t)$ is the base acceleration (in this case, of the bearing housing), and $v(t)$ is the output voltage. For more details, refer to [54, 55].

The electrical circuit used as an analog system to compute the HI for the bearing condition is illustrated in Figure 4. The signal generated by the PEH passes through a resistance $R$, which limits the current $i$, before entering a diode bridge that rectifies the signal. At the output of the rectifier, a capacitor $C_l$ stores the rectified signal over a predefined period of time, this energy is the HI. This stored energy represents the HI. A switch controls the charging and discharging of the capacitor, and

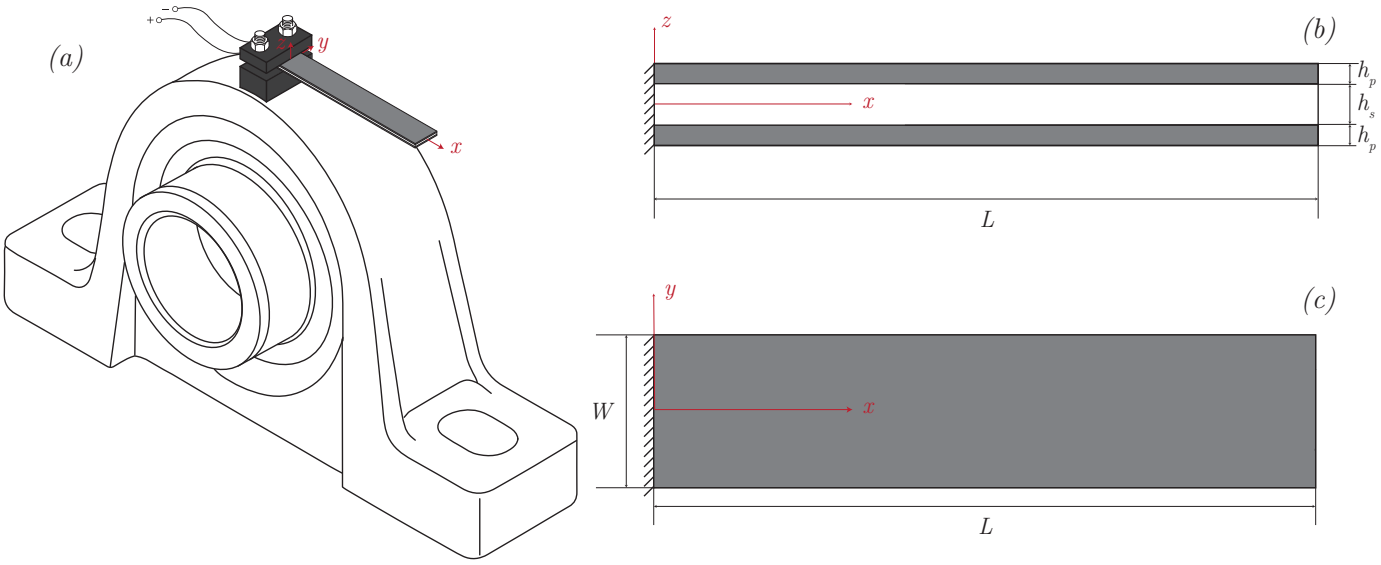


Figure 3: ($a$) Schematic representation of the PEH mounted on a bearing housing. Additionally, the PEH is illustrated as a cantilever plate composed of two piezoelectric layers and a central substructure layer, shown in the ($b$) side view and ($c$) top view.

the stored energy is dissipated through a load resistor $R_l$ between measurement intervals. This energy can be effectively measured using an oscilloscope, as it corresponds to the instantaneous voltage across the capacitor, according to the following equation:

$$E = \frac{1}{2} C v_c^2 \tag{3}$$

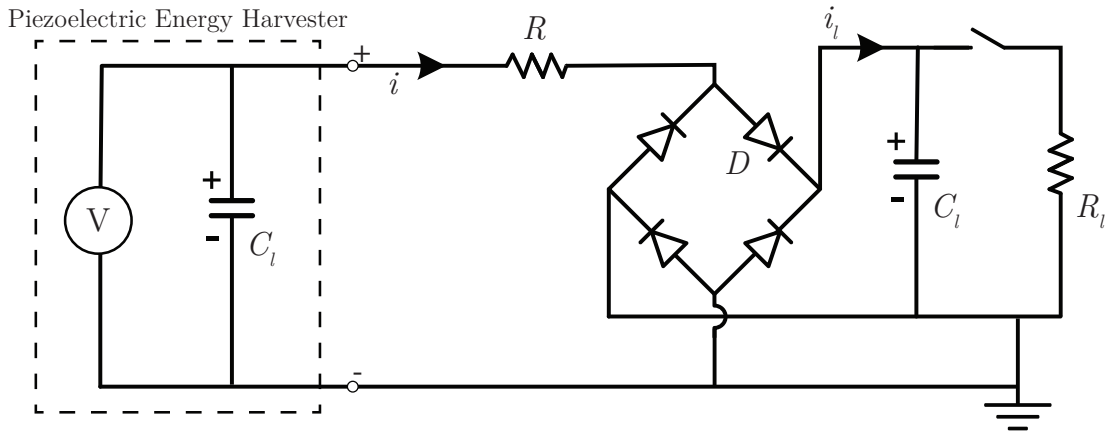


Figure 4: ($a$) Schematic representation of the PEH mounted on a bearing housing. Additionally, the PEH is illustrated as a cantilever plate composed of two piezoelectric layers and a central substructure layer, shown in the ($b$) side view and ($c$) top view.

The system is modelled using a Simulink block diagram to estimate the voltage accumulated in the capacitor by solving a state-space formulation (Eq. 4) with MATLAB's `ode45` solver. This formulation integrates the dynamic equations with electrical coupling and incorporates the circuit equations that account for mechanical interactions. As a result, it provides a comprehensive representation of the

system's electromechanical behavior as,

$$\dot{\mathbf{x}} = \boldsymbol{A}\mathbf{x} + \boldsymbol{B}\mathbf{u} \tag{4}$$

where $\mathbf{x} = \{\mathbf{w}(t) \quad \dot{\mathbf{w}}(t) \quad v(t)\}$ is the state-space vector, $\mathbf{u} = \{a(t) \quad i(t)\}$ is the input vector and the matrices $\boldsymbol{A}$ and $\boldsymbol{B}$ are defined as follows,

$$\boldsymbol{A} = \begin{bmatrix} \mathbf{0}_{N\times N} & \mathbf{M}_{N\times N} & \mathbf{0}_{N\times 1} \\ -\mathbf{K}_{N\times N} & -\mathbf{C}_{N\times N} & \boldsymbol{\Theta}_{N\times 1} \\ \mathbf{0}_{1\times N} & -\frac{\boldsymbol{\Theta}_{1\times N}^T}{C_p} & 0 \end{bmatrix}, \quad \boldsymbol{B} = \begin{bmatrix} \mathbf{0}_{N\times 1} & \mathbf{0}_{N\times 1} \\ \mathbf{F} & \mathbf{0}_{N\times 1} \\ 0 & C_p^{-1} \end{bmatrix} \tag{5}$$

In the particular case where the base acceleration is a harmonic signal, given by $a_b(t) = A_b e^{i\omega t}$ (with $i = \sqrt{-1}$), and the PEH is directly connected to a resistive load $R_l$ — such that $i(t) = v(t)/R_l$ — the output voltage also exhibits harmonic behavior and can be expressed as $v(t) = V_o e^{i\omega t}$. The Frequency Response Function (FRF), denoted by $H = H(\omega)$, can then be defined to relate the amplitude of the output voltage $V_o$ to the amplitude of the excitation acceleration $A_b$ at a given frequency $\omega$, based on Equations (1) and (2).

$$H(\omega) = i\omega \left(\frac{1}{R_l} + i\omega C_p\right)^{-1} \boldsymbol{\Theta}^T \boldsymbol{\Phi}_o \left(-\omega^2 \mathbf{I}_o + j\omega \mathbf{c}_o + \mathbf{k}_o + i\omega \left(\frac{1}{R_l} + i\omega C_p\right)^{-1} \boldsymbol{\theta}_o \boldsymbol{\Theta}^T \boldsymbol{\Phi}_o\right)^{-1} \mathbf{f}_o \tag{6}$$

## 3. Intelligent Maintenance System (IMS) database

The Intelligent Maintenance Systems (IMS) database, developed at the University of Cincinnati, is one of the most extensively used public datasets for research on bearing fault diagnosis. Figure 5 shows the test bench used in the IMS dataset, which consists of a shaft supported by four bearings (Rexnord ZA-2115 model), an AC motor coupled to the shaft via rubber belts, and a spring mechanism that applies a radial load of 6000 lbs to the shaft and bearings.

The database contains vibration data from four bearings across three run-to-failure (lifetime) datasets. In all cases, bearing failures occurred after exceeding their designed lifetime of over 100 million revolutions. In Set 1, two accelerometers were installed on each bearing housing to capture vibrations in both the x- and y-directions. In contrast, Sets 2 and 3 used only one accelerometer per bearing. A NI DAQCard-6062E was used to acquire data at a sampling rate of 20 kHz. Each dataset consists of approximately 1 second of acceleration data (20,480 points), recorded every 10 minutes.

Table 1: Specifications of the bearing used in the IMS database, Rexnord ZA-2115 [7]

| | |
|---|---|
| Pitch diameter ($D$) | 71.5 mm (2.815 inch) |
| Rolling element diameter ($d$) | 8.4 mm (0.331 inch) |
| Number of rolling elements per row ($n$) | 16 |
| Load contact angle ($\phi$) | 15.17° |
| Static load ($Q$) | 26,690 N (6,000 lbs) |
| Shaft angular velocity ($\omega$) | 2,000 rpm |

Set 2 is selected to analyze the capability of the proposed electrical circuit to capture the trend of bearing degradation. The rationale behind choosing this set is its extensive coverage in the literature. In particular, numerous studies have focused on identifying the Early Fault (EF) point, which marks

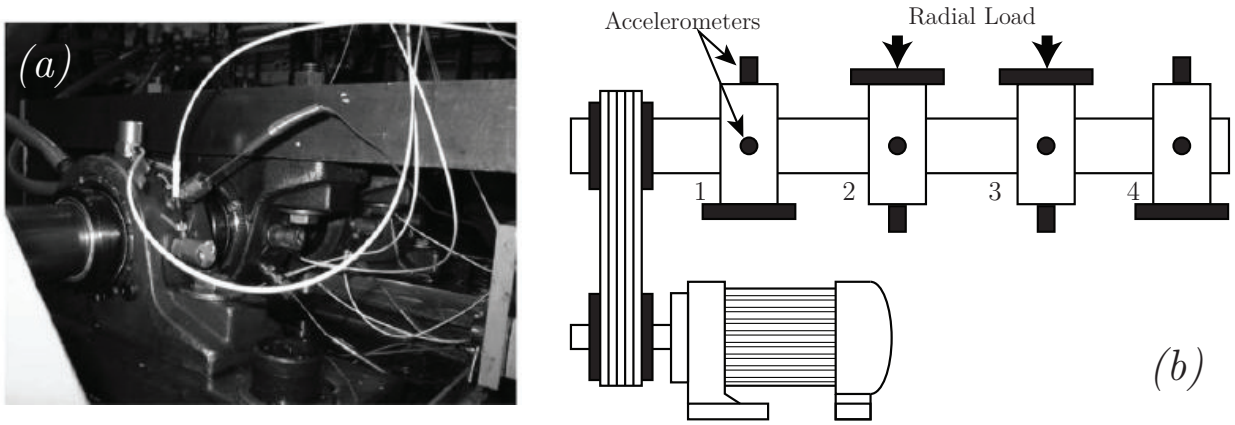


Figure 5: ($a$) Test rig from the IMS database. ($b$) An illustration of the accelerometer placement (left), adapted from [56].

the onset of slow degradation in the bearing. These works propose various methodologies and report EF point estimates, as summarized in Table 2. Specifically, it has been observed that the EF point lies within the range of samples 487 to 610, with a general consensus around sample 533, which is adopted as the reference point in this study.

Table 2: Early fault detection reported for set 2 of the IMS database in the literature.

| Reference | Reported EF | Year | Reference | Reported EF | Year | Reference | Reported EF | Year |
|---|---|---|---|---|---|---|---|---|
| [57] | 533 | 2024 | [58] | 523 | 2021 | [59] | 535 | 2019 |
| [37] | 533 | 2024 | [60] | 532 | 2020 | [61] | 610 | 2019 |
| [62] | 487 | 2023 | [**?** ] | 535 | 2020 | [63] | 540 | 2019 |
| [64] | 523, 639 | 2022 | [65] | 532 | 2020 | [66] | 609 | 2018 |
| [67] | 532 | 2021 | [68] | 483 | 2019 | [69] | 533 | 2017 |

As previously discussed, the RMS of the acceleration signal is an effective metric for describing the trend of bearing degradation and is therefore used as a reference in this study. In a initial approach, the proposed electrical circuit is driven by a voltage signal equivalent to the acceleration signal—rather than the voltage generated by the PEH—allowing a direct comparison of its effectiveness in capturing the bearing degradation process. To ensure a meaningful comparison between the two HI, the data are normalized. In the context of bearing fault diagnosis, it is standard practice to assess the current condition of a mechanical component relative to a reference or baseline state. In this study, the first 144 samples—corresponding to one day of operation—are designated as the baseline. Accordingly, the Relative Health Indicator (RHI) is calculated using the mean value $\mu_{\text{baseline}}$ obtained from this period, according to the following equation:

$$\text{RHI}(i) = \frac{\text{HI}(i)}{\mu_{baseline}}, \quad \mu_{baseline} = \frac{1}{M}\sum_{i=1}^{M}\text{HI}(i) \tag{7}$$

Figure 6 presents a comparison between the two RHIs, showing strong agreement between them. This suggests that methodologies based on RMS can be directly applied to the proposed Health Indicator. It is possible to identify the three degradation stages and observe the characteristic trends that the RHI follows in each stage. It is important to note that, in this analysis, the acceleration signal

was used as the input to the circuit, whereas the primary objective of this study is to demonstrate that a piezoelectric cantilever signal can be used to power the system. This aspect will be examined in the following sections, using the RMS-based RHI as a reference to evaluate the effectiveness of the proposed approach.

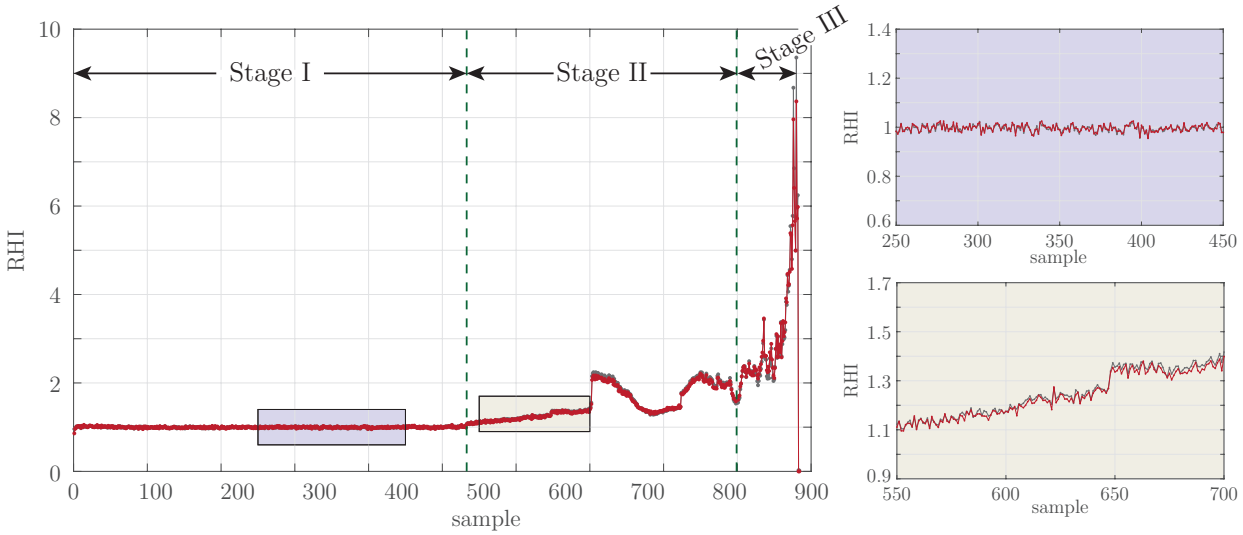


Figure 6: Degradation trajectory of a bearing from Set 2 of the IMS dataset, comparing the evolution of the proposed Relative Health Indicator (RHI) (red) with the traditional Relative RMS-based indicator (gray). The three degradation stages are indicated, along with zoomed-in views highlighting the behaviour during Stage I and Stage II.

## 4. Case Study: Piezoelectric Cantilever-Based Analog Computing of Health Indicators in the IMS Dataset

This section presents the experimental validation of the proposed PEH-based analog framework for HI computation. The system leverages the energy generated by a PEH to compute the HI directly in the analog domain, without the need for an external power source. To assess its effectiveness, the framework is tested on a well-established case study using the IMS bearing dataset, a publicly available benchmark widely adopted in the condition monitoring community. This choice enables direct comparison and adoption with previous methods and supports a robust evaluation. The objective of this case study is to demonstrate the system's capability to track bearing degradation and identify key milestones in the process, including the early fault point, the elbow point (onset of accelerated degradation), and the remaining useful life (RUL).

The design of the PEH plays a critical role in the performance of the proposed analog system, as it directly influences the harvester's resonant frequency. This frequency determines the range of vibrational components from the bearing housing that are most efficiently converted into electrical energy. As a result, the energy accumulated in the capacitor, and consequently the computed HI,is inherently sensitive to spectral variations occurring near the PEH's resonance. This means that the system acts as a passive spectral filter, emphasising changes in a specific frequency band of the acceleration signal. Therefore, selecting an appropriate PEH design is essential to ensure that the monitored frequency range captures relevant fault-related features in the vibration response.

In rotary bearings, the presence of localised defects results in characteristic fault frequencies that appear as distinct spectral components in the vibration signal. These include the ball-on-the-outer-race pass frequency (BOPF), the ball-on-the-inner-race pass frequency (BIPF), the ball-flipping frequency (BSF), and the fundamental train frequency (FTF), each associated with a specific failure mode. Given that the PEH acts as a passive, frequency-selective filter, its design can be tailored to enhance sensitivity to one or more of these fault-related components. By tuning the resonant frequency of the PEH to coincide with a targeted characteristic fault frequency, the analog system becomes inherently responsive to the emergence and evolution of the corresponding damage mechanism. As a result, the harvested energy, and the HI derived from it, can serve as an indirect yet effective measure of bearing condition, even without full-spectrum acquisition or digital post-processing. The characteristic frequencies of interest can be expressed as follows,

$$\text{BPFO} = \frac{nf_r}{2}\left(1 - \frac{d}{D}cos(\phi)\right) \tag{8}$$

$$\text{BPFO} = \frac{nf_r}{2}\left(1 + \frac{d}{D}cos(\phi)\right) \tag{9}$$

$$\text{BSF} = \frac{f_r D}{2d}\left(1 - \left(\frac{d}{D}cos(\phi)\right)^2\right) \tag{10}$$

The characteristic fault frequencies in rolling bearings are determined by their geometric properties. For the IMS dataset used in this study, these geometric properties are listed in Table 1, and the resulting characteristic fault frequencies are presented in Table 2.

To design the PEH with an adequate diagnostic sensitivity, its resonant frequency must be carefully selected to align with the spectral content associated with bearing characteristic fault frequencies. For this purpose, an average vibration spectrum is computed using the first 144 samples of the dataset, representing one day of baseline operation. Figure 7 presents the average spectrum, which reveals

Table 3: Characteristic frequencies of the IMS test rig [7]

| | |
|---|---|
| Nominal rotation frequency ($f_r$) | 33. 3 Hz |
| Ball Pass Frequency Outer Race (BPFO) | 236 Hz |
| Ball Pass Frequency Inner Race (BPFI) | 297 Hz |
| Ball Spin Frequency (BSF) | 139 Hz |
| Fundamental Train Frequency (FTF) | 15 Hz |

the presence and distribution of their harmonics while the characteristic fault frequencies are also indicated. The selection of the PEH's resonant frequency is guided by two main criteria: proximity to one or more fault-related frequencies, and location within a region of the spectrum where the amplitude of background vibrations is relatively low. This strategy aims to enhance the sensitivity of the system to incipient faults while minimising the influence of natural variability and operational noise. In the present study, the third harmonic of the BPFO (3×BPFO) is selected as the target frequency. This choice is justified by its alignment with a key fault frequency and its position within a low-amplitude region of the baseline spectrum. While this selection is specific to the analysis of Set 2 in the IMS database, the methodology is generalisable.

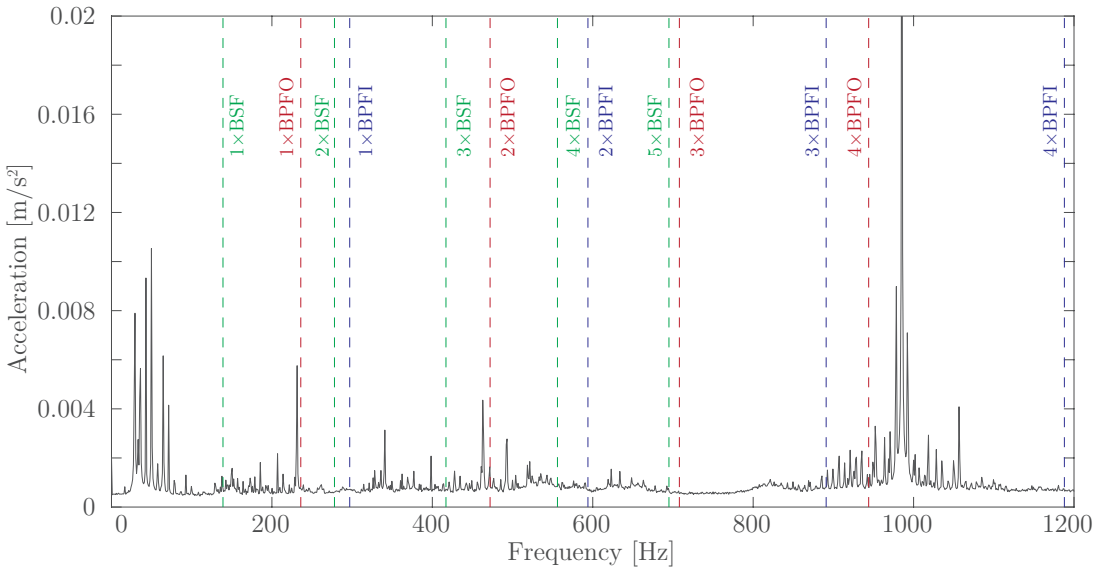


Figure 7: Averaged vibration spectrum computed from the first 144 samples of Set 2 in the IMS dataset, representing baseline operating conditions. The characteristic fault frequencies of the bearing are indicated by vertical dashed lines in red (BPFO), blue (BPFI), and green (BSF).

Therefore, the PEH design consists of two PZT-5A layers bonded to both sides of a steel substructure. The device is designed to achieve a natural frequency of 708 Hz, corresponding to the third harmonic of the BPFO (3×BPFO). Specifically, the thicknesses of the piezoelectric layers ($h_p$) and the substructure ($h_s$) are both set to 1 mm, with a width ($W$) of 50 mm and a length ($L$) of 3.9 mm. With the PEH design established, the following subsections examine the capability of the analog-computed HI to identify key milestones in the bearing degradation process.

*4.1. Early Fault Detection*

The aim of this section is to assess the capability of the PEH-based analog-computed HI to detect the early fault point in the bearing degradation process. The ability to identify faults at their earliest stages is a cornerstone of effective predictive maintenance, offering significant benefits in terms of operational efficiency and system reliability. The approach proposed here is designed with online monitoring in mind, relying on the advantage already discussed of low-power, analog signal processing by being embedded directly into the machine's structure, thereby eliminating the need for high-frequency data acquisition or complex digital analysis.

To identify the EF point using the PEH-based analog-computed HI, this work adopts the slope-change detection algorithm originally proposed by Yan et al. [9]. The algorithm fits a linear regression $y = kx + b$ within a sliding window of HI values to estimate the local trend. This enables the computation of the detrended HI sequence, denoted as $\mathrm{HI}_d(j)$, which represents the HI values of sample $j$ after removing the local trend (as defined in Equation 11). Subsequently, the upper bounds of this detrended sequence are calculated based on the standard deviation $\sigma$ and mean value $\mu$, as shown in Equation 12.

$$\mathrm{HI}_d(j) = \mathrm{HI}(j) - k \cdot x_j - b \tag{11}$$

$$\mathrm{HI}_{ub}(j) = k \cdot x_j + b + Inc \cdot \sqrt{1 + k^2} \cdot \sigma \tag{12}$$

where

$$\sigma = \sqrt{\frac{1}{n} \sum_{j=1}^{n} [\mathrm{HI}_d(j) - \mu]^2} \tag{13}$$

and

$$\mu = \frac{1}{n} \sum_{j=1}^{n} \mathrm{HI}_d(j) \tag{14}$$

The EF point marks the transition between the normal operating condition and the onset of slow degradation, where the slope of the HI changes from a near-zero value to a consistently increasing trend. The procedure of the detection algorithm is illustrated in Figure 8, which highlights the mean value, upper bound, and sliding window used for monitoring. To improve the robustness of the algorithm against spurious fluctuations, a slope variation is marked only when the values of the HI exceed the upper bound of the sliding window in $m$ consecutive instances. An example of this behaviour is illustrated in Figure 8. Once two successive slope increments are detected, the transition to slow degradation is confirmed, and the slow degradation is identified.

The selection of both the sliding window length $W_{len}$ and the number of consecutive exceedances $m$ is critical, as these parameters directly influence the accuracy and sensitivity of the fault detection algorithm. For instance, Yan et al. [9] observe that the fluctuation of the slope (when using RMS as the HI) tends to decrease as the window length increases. Following the recommendations provided in that study, $W_{len}$ and $m$ are adopted as 40 and 5, respectively, as suitable parameter values in this work. On the other hand, Inc is the multiplier of the standard deviation $\sigma$ used to define the upper bound. In Yan et al. [9], it is set to 1.8. However, in this work, a more stringent threshold is required, as the transition to slow degradation is more subtle. Therefore, $Inc$ is set to 1. In addition, before applying the methodology, the HI is post-processed using the Inertial Relative Health Indicator IRHI proposed in [70], which helps reduce spurious fluctuations. The IRHI is computed based on the RHI, defined in Equation 7, and the $\mathrm{HI}_d$, defined in Equation 11. Note that the calculation of $\mathrm{HI}_d$ requires

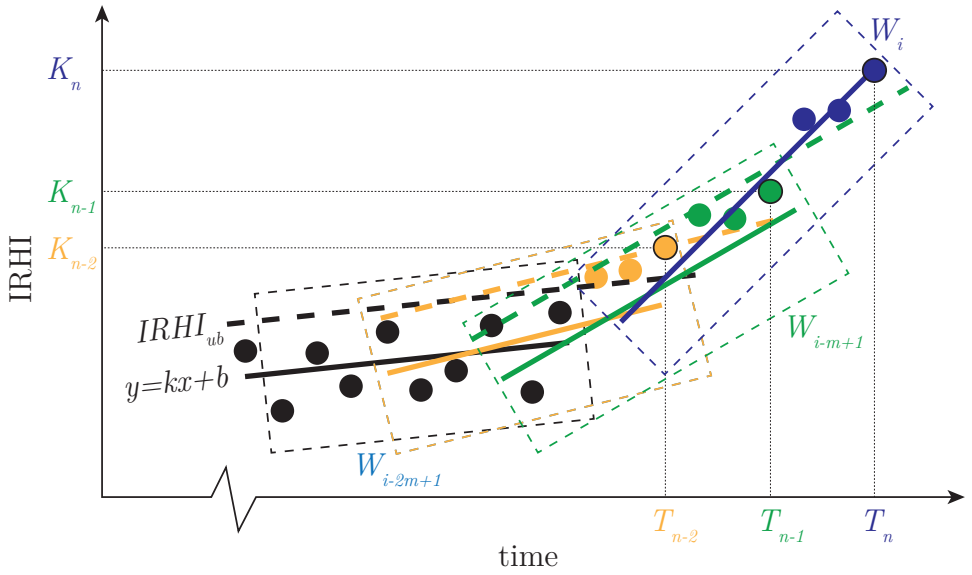


Figure 8: Illustration of the adapted algorithm for detecting changes in the degradation trend of bearings, originally proposed by Yan et al. The figure is reproduced with modifications from [9].

the definition of a sliding window. Following the recommendation in [9], a window length of 30 is used. The expression is given by,

$$\mathrm{IRHI}(i) = \begin{cases} \frac{1}{n}\sum_{j=1}^{n} \mathrm{RHI}(j), & \text{if } \mathrm{RHI}_d(i) \leq \mu - 3\sigma \\ k \cdot x_i + b, & \text{if } \mu - 3\sigma < \mathrm{RHI}_d(i) < \mu + 3\sigma \\ k \cdot x_i + b + \mu + 3\sigma, & \text{if } \mathrm{RHI}_d(i) \geq \mu + 3\sigma \end{cases} \tag{15}$$

Figure 12 presents the results of applying the trend change detection algorithm to Bearing 2 from the IMS dataset (Set 2). The RHI is shown in grey, while the IRHI is shown in black. As observed, the IRHI effectively suppresses spurious fluctuations, offering a smoother trend suitable for reliable monitoring. The slope-based methodology is applied to the IRHI curve, successfully detecting the onset of slow degradation at sample 595, which would serve as the online detection point. However, this does not necessarily correspond to the true start of the degradation. To estimate the actual initiation of the fault, a retrospective linear regression is applied within the current sliding window to identify the point where the extrapolated IRHI reaches the baseline value (IRHI = 1). This analysis indicates that the slow degradation likely began around sample 532, which closely aligns with the consensus value of 533 reported in the literature and summarized in Table 2 of the previous section.

### *4.2. Elbow point detection*

The objective of this section is to demonstrate that the elbow point, marking the transition from slow to accelerated degradation, can be effectively identified using the analog-computed Health Indicator. The detection algorithm employed here is the same as that described in the previous section; however, the threshold parameter Inc, which defines the confidence bounds for trend deviation, is adjusted. In the previous section, a lower value of Inc = 1 was used to detect subtle early-stage changes in the degradation curve. In this case, a value of Inc = 1.8, as originally proposed in [9], is adopted to detect the more pronounced slope change associated with the elbow point. This adjustment aligns the methodology with its original purpose and enables a fair assessment of its applicability to the analog-computed metric.

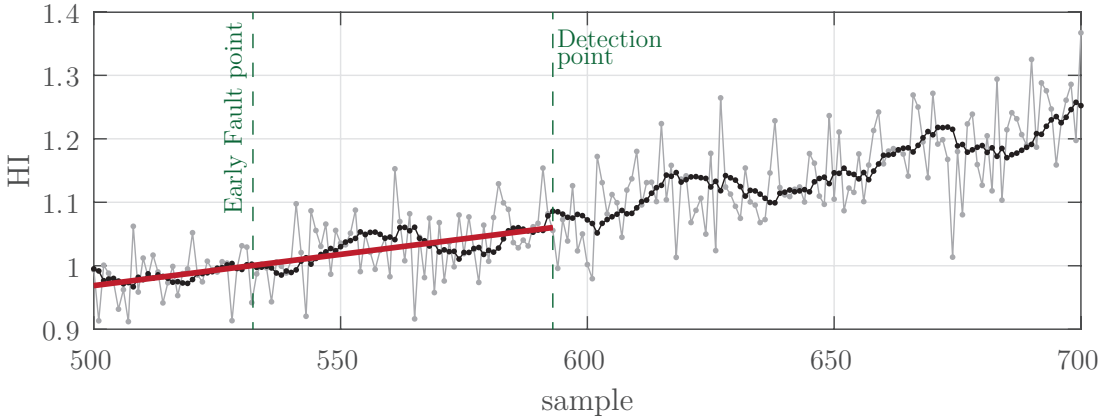


Figure 9: Implementation of the trend change detection algorithm on Bearing 2 from the IMS dataset (Set 2). Two key points are identified in the IRHI degradation curve: (1) the online monitoring detection point, determined by the algorithm, and (2) the early fault point, estimated retrospectively via linear regression to the baseline value (IRHI = 1).

Applying the methodology with Inc = 1.8, the onset of accelerated degradation is identified at sample 890 using the analog-computed HI. This point precedes the value commonly reported in the literature, which places the elbow point around sample 900. However, this slight anticipation is not necessarily problematic, as long as the method enables accurate RUL estimation from that point onward. In fact, when following the trend deviation method further, it is possible to retrospectively estimate the elbow point by backward projection, locates the elbow point at sample 861.

### *4.3. RUL estimation*

Once the elbow point has been identified, marking the onset of the accelerated degradation phase, the primary objective shifts to the estimation of the RUL. Reliable RUL prediction is fundamental for implementing effective maintenance strategies. As previously discussed, this capability not only enables optimal scheduling of maintenance interventions—thereby preventing unplanned downtime and minimising operational costs, but also significantly enhances system safety and reliability by ensuring timely preventive actions. This section evaluates the capability of the proposed analog-computed Health Indicator to support accurate RUL estimation under realistic operating conditions.

Yan et al [9] proposed an approach based on the fitting of a degradation model using a sliding window of HI values, with RMS as the chosen HI in their implementation. Before the fitting, the HI data is smoothed following a rule based on two bounds defined by two regression models, as illustrated in Figure 10. When a new sample's value exceeds the upper bound (point $a$ in Figure 10), the smoothed sample is set to the upper bound. If the new sample is between the two bounds (point $b$ in Figure 10), the smoothed sample remains unchanged. Otherwise, if the new sample is lower than the lower bound (point $c$ in Figure 10), the sample moves to the midpoint between the two bounds. The lower bound is defined by a linear fitting $y = kx + b$ within a sliding window, while the upper bound is obtained from a nonlinear fitting $y = Y + Mx^{\beta}$, also computed within the sliding window. This approach thus enables the interpolation of the degradation process using the regression model, $y = Y + Mx^{\beta}$, and the estimation of the time required to reach a predefined failure threshold. For more details refer to [9].

The RUL estimation methodology described above is applied to the analog-computed metric using the RHI defined in Equation 7. Before presenting the RUL prediction results, it is important to clarify the definition of the failure threshold. In implementations using RMS as the Health Indicator, failure

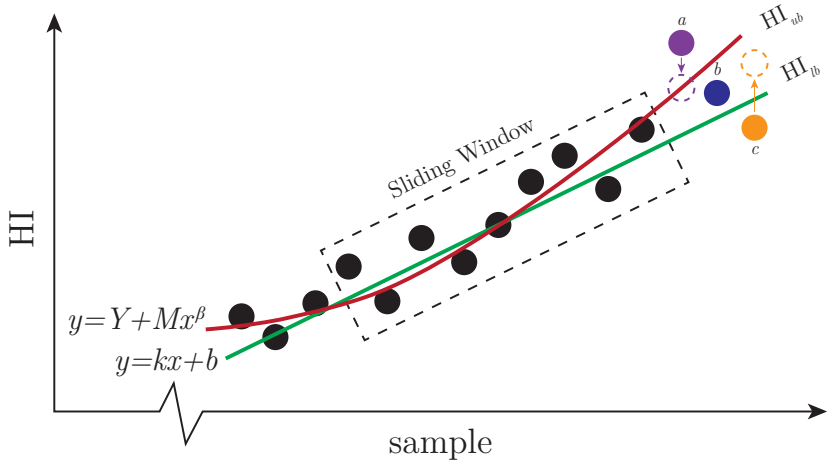


Figure 10: Illustration of the HI smoothing process. Points $a$, $b$, and $c$ illustrate different scenarios relative to the estimated bounds, with $HI_{ub}$ and $HI_{lb}$ defining the upper and lower limits of the samples, respectively. The upper bound is defined by the nonlinear model $y = Y + Mx^{\beta}$ (red curve), while the lower bound is represented by the linear approximation $y = kx + b$ (green line). The figure is reproduced with modifications from [9].

is typically defined by a fixed threshold—set to 13 in the IMS database—which, for this specific test case, results in a predicted failure point at sample 978. However, since the analog-computed metric (RHI) operates on a different scale, this threshold cannot be directly transferred. To ensure consistency and comparability, the failure threshold for the RHI is adjusted so that failure is also predicted at sample 978. This led to the selection of a threshold value of 34 for the RHI, thereby maintaining the same failure reference point across both metrics. Figure 13 presents the RUL prediction process based on the RHI at three distinct sample points. The smoothed RHI values used for each regression are shown in red, while the fitted exponential curves, which capture the progression of degradation, are shown in black. As degradation evolves, the predicted RUL converges toward the actual RUL, demonstrating the method's capability for accurate prognostics. In all three cases, the fitted model remains stable and well-aligned with the observed trend, confirming the robustness of the approach. The green dashed lines indicate the estimated and actual failure points, which remain consistently close to the true failure location, reinforcing the viability of the proposed method for real-time RUL estimation.

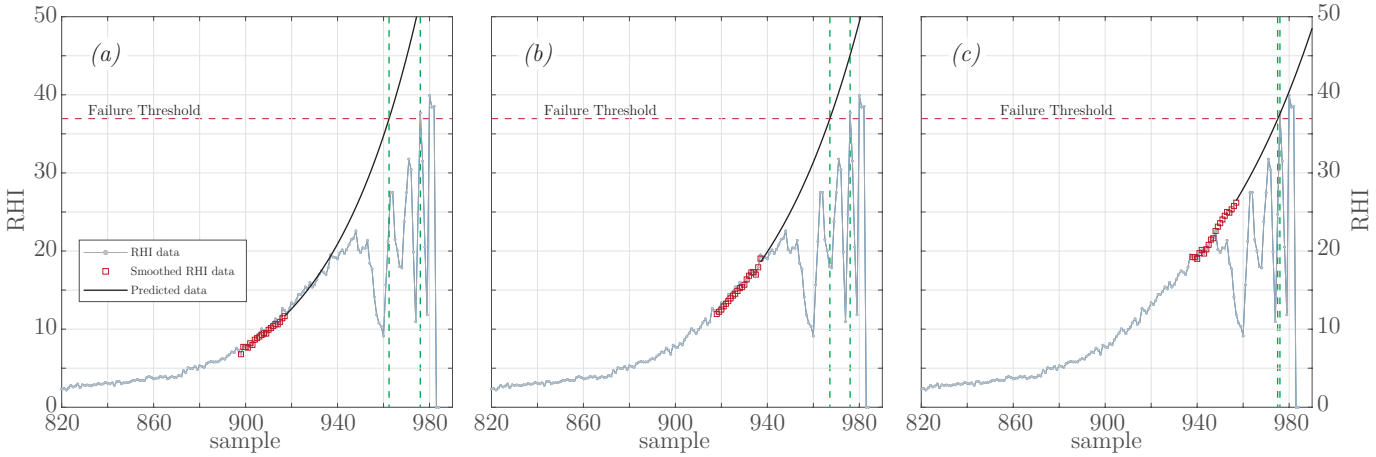


Figure 11: RUL prediction process based on the evolution of the RHI at sample: ($a$) 917, ($b$) 937, ($c$) 957

Figure 12 compares the RUL predictions at each time step during the degradation process, enabling an online monitoring perspective. The proposed analog-computed Health Indicator (blue squares) is evaluated against the RMS-based method reported in [9] (2022) (red circles). Both predictions are compared to the current RUL (solid black line), with dashed lines indicating ±25% tolerance limits. The results show that the analog-computed metric delivers RUL predictions that are consistently comparable to those obtained using high-frequency, digitally processed RMS signals. Notably, the analog approach maintains its predictions within the 25% tolerance band across the almost entire prediction horizon, demonstrating its reliability despite relying on low-power analog signal processing. Additionally, the analog-computed predictions are slightly more conservative during the early degradation phase, which may be advantageous in critical systems where early and cautious fault response is preferred. As degradation progresses, both methods converge toward the current RUL, confirming the suitability of the proposed method for real-time, low-resource prognostics without compromising prediction accuracy.

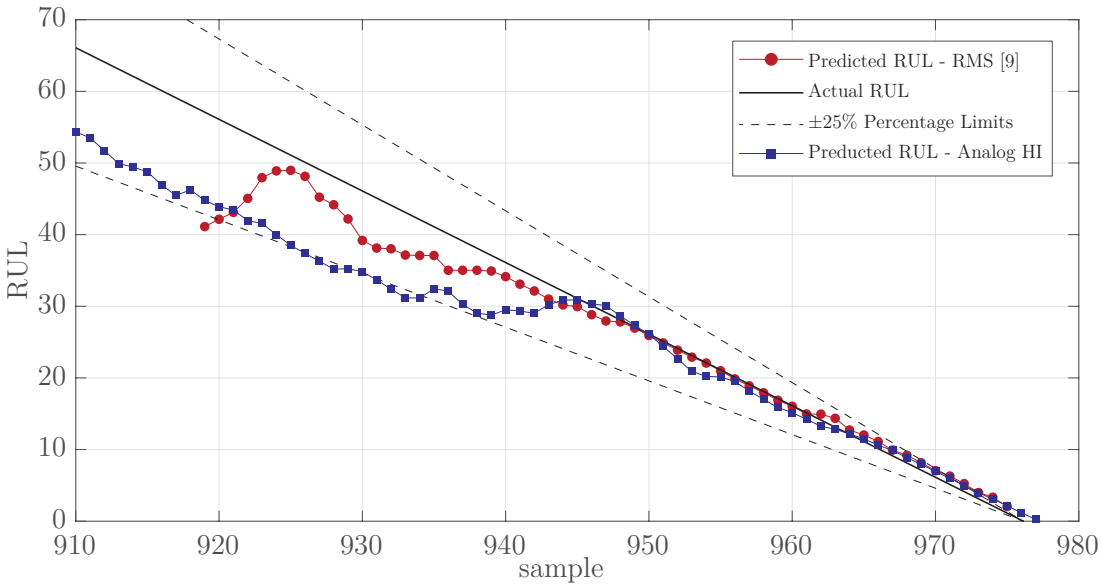


Figure 12: Comparison of RUL predictions based on the analog-computed Health Indicator (blue squares) and the RMS-based method reported in [9] (red circles). The solid black line represents the actual RUL, while the dashed lines indicate ±25% tolerance limits.

## 5. Evaluating the Energy Efficiency

As previously discussed, fault detection methods generally prioritise classification accuracy, but their practical deployment is often constrained by the energy and data demands associated with high-frequency vibration acquisition and wireless transmission. This section aims to quantify the energy consumption savings related to data acquisition and transmission of the proposed framework compared to a recent state-of-the-art method from the literature. Specifically, this study benchmarks the method presented by Shi et al., which analyses the electrical output of a piezoelectric device using a CNN-based framework. In their framework, the sampling frequency $f_s$ is set at 50 kHz, and the acquisition time is 20 seconds. Additionally, this analysis considers an observation period $T_{obs}$ of 10 minutes, referencing the IMS dataset. In contrast, the proposed framework requires only one sample to evaluate the bearing condition, which is equivalent to sampling frequency $f_s$ of 0.05 Hz.

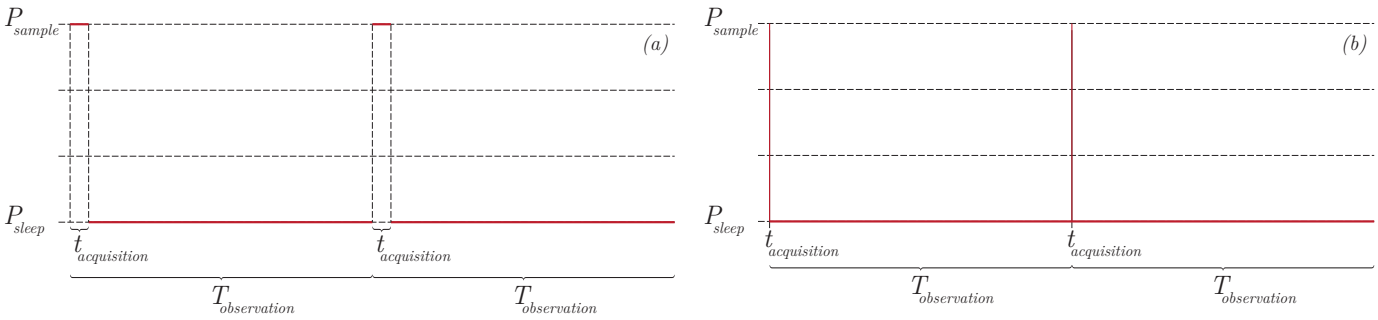


Figure 13: Qualitative comparison of power consumption profiles between ($a$) a conventional high-frequency sampling strategy and ($b$) the proposed ultra-low sampling frequency approach.

To quantify the power consumption during sampling, an electronic system based on the Texas Instruments SensorTag7 is considered. This device features an ultra-low-power ARM Cortex-M3 MCU. According to Lan et al., the power consumption during sampling ($P_{sample}$) and in sleep mode ($P_{sleep}$) for this system are 480 $\mu$W and 6 $\mu$W, respectively. Additionally, the duration of time required by the MCU to complete a single voltage sample (tsample) is 0.6 ms. This implies a maximum sampling frequency of 1.66 kHz for duty-cycled operation, which is significantly lower than the benchmark method's sampling frequency of 50 kHz. As a result, this analysis may under-estimate the energy savings associated with sensing tasks.

Thus, the average observation power consumption ($P_{av}$) during the observation period for the benchmark framework, considering an acquisition time ($t_{acq}$) of 20 seconds and a sleep time ($t_{sleep}$) of 580 seconds, is 21.9 $\mu$W. Meanwhile, in the proposed framework, where the acquisition time is 0.6 ms because only a single sample is necessary to evaluate the bearing condition, the average power consumption (Pav) is 6.005 $\mu$W. This results in energy consumption savings in sensing of approximately 72.5%. These savings can be even higher if the observation period is reduced. This information is summarised in Table 4.

A similar analysis can be conducted for wireless transmission, utilising a BLE beacon for broadcasting information. The CC2650 wireless MCU is programmed to periodically wake up and transmit a BLE beacon packet. Each sample is transmitted three times across three separate channels to enhance broadcasting reliability. The beacon packets range from 19 to 28 bytes. Four states are identified in the broadcasting process: Radio setup $S_i$, Radio transmission of a beacon packet $S_t$, Transition between transmissions $S_g$, and Post-processing $S_f$.

The amount of data transmitted in the benchmark framework is 1 million samples (50 kHz $\times$ 20 s), which corresponds to 2 million bytes. Given that the maximum payload of a single BLE beacon is 28

Table 4: Energy consumption for data acquisition: benchmark vs. proposed method.

| | Benckmark | Proposed |
|---|---|---|
| Frequency Sample ($f_s$) | 50 kHz | 0.05 Hz |
| Average Sampling Power ($P_{sample}$) | 480 $\mu$W | 480 $\mu$W |
| Average Sleep Power ($P_{sleep}$) | 6 $\mu$W | 6 $\mu$W |
| Acquisition Time ($t_{ac}$) | 20 s | 0.6 ms |
| Sleep Time ($t_{sleep}$) | 580 s | 599.9994 s |
| $E_{da}$ | 13.08 mJ | 3.6 mJ |

Table 5: Time duration and power consumption associated with each state involved in the BLE beacon broadcasting process.

| State | Time (ms) | Power ($\mu$W) |
|---|---|---|
| Radio setup ($S_i$) | 1.12 | 1008 |
| Radio transmission of a beacon packet ($S_t$) | 0.28 | 3990 |
| Inter-transmission gap ($S_g$) | 0.30 | 2460 |
| Post-processing ($S_f$) | 1.72 | 744 |

bytes, a total of 71,429 packets (2,000,000 / 28) are required. As a result, the total energy consumption amounts to 0.59 J over a transmission duration of 172.29 seconds. Notably, this duration exceeds the original acquisition time, indicating that a transmission buffer would be necessary in the system. In contrast, the proposed framework only transmits 2 bytes, resulting in an energy consumption of 7.42 $\mu$J and a transmission time of 4.33 ms, yielding an energy saving of 99.998%.

These results related to the system's energy consumption suggest that a significant reduction in data acquisition and transmission requirements can be achieved using the proposed methodology. This opens the possibility of partially or even fully powering the system using the energy harvested by the piezoelectric device. However, this depends on the specific design of the harvester, which not only determines the energy output but also directly impacts the sensing performance, as discussed in Section V. Therefore, careful consideration must be given to the selection or design of the PEH to balance both energy supply and monitoring reliability. Although the energy harvested may not always be sufficient for continuous operation, the low power demands of the proposed system make it feasible to achieve long-term operation when supported by a battery-assisted setup. In such configurations, the harvested energy contributes to extending battery life, especially when combined with an additional energy harvesting system.

## 6. Conclusions

This work introduces and validates a PEH-based analog system for bearing fault diagnosis that combines energy harvesting with health indicator computation. The main findings are:

- The energy stored in the PEH's capacitor correlates strongly with conventional RMS-based indicators, allowing accurate detection of degradation stages.
- The proposed system successfully identifies the early fault point, elbow point, and provides reliable RUL predictions comparable to digital high-frequency approaches.

- Significant energy savings in both data acquisition and transmission are demonstrated, highlighting the feasibility of autonomous, long-term operation

Overall, the study confirms the potential of PEH-based analog computing as an enabling technology for self-powered smart bearings and energy-efficient condition monitoring systems.

## References


[1] C. He, P. Han, J. Lu, X. Wang, J. Song, Z. Li, S. Lu, Real-time fault diagnosis of motor bearing via improved cyclostationary analysis implemented onto edge computing system, IEEE Transactions on Instrumentation and Measurement (2023).

[2] Y. Jin, L. Hou, Y. Chen, A time series transformer based method for the rotating machinery fault diagnosis, Neurocomputing 494 (2022) 379–395.

[3] Senseye, The true cost of downtime 2022, 2022. Accessed: 2025-01-16.

[4] X. Xu, Z. Tao, W. Ming, Q. An, M. Chen, Intelligent monitoring and diagnostics using a novel integrated model based on deep learning and multi-sensor feature fusion, Measurement 165 (2020) 108086.

[5] S. Mushtaq, M. M. Islam, M. Sohaib, Deep learning aided data-driven fault diagnosis of rotatory machine: A comprehensive review, Energies 14 (2021) 5150.

[6] M. Tiboni, C. Remino, R. Bussola, C. Amici, A review on vibration-based condition monitoring of rotating machinery, Applied Sciences 12 (2022) 972.

[7] D. Sacerdoti, M. Strozzi, C. Secchi, A comparison of signal analysis techniques for the diagnostics of the ims rolling element bearing dataset, Applied Sciences 13 (2023) 5977.

[8] Y. Zhang, J. Sun, J. Zhang, H. Shen, Y. She, Y. Chang, Health state assessment of bearing with feature enhancement and prediction error compensation strategy, Mechanical Systems and Signal Processing 182 (2023) 109573.

[9] M. Yan, L. Xie, I. Muhammad, X. Yang, Y. Liu, An effective method for remaining useful life estimation of bearings with elbow point detection and adaptive regression models, ISA transactions 128 (2022) 290–300.

[10] Z. Wang, Y. Ta, W. Cai, Y. Li, Research on a remaining useful life prediction method for degradation angle identification two-stage degradation process, Mechanical Systems and Signal Processing 184 (2023) 109747.

[11] P. Ding, M. Jia, X. Yan, Stationary subspaces-vector autoregressive with exogenous terms methodology for degradation trend estimation of rolling and slewing bearings, Mechanical Systems and Signal Processing 150 (2021) 107293.

[12] Y. Wang, Y. Peng, Y. Zi, X. Jin, K.-L. Tsui, A two-stage data-driven-based prognostic approach for bearing degradation problem, IEEE Transactions on industrial informatics 12 (2016) 924–932.

[13] J. Yuan, Y. Wang, Y. Peng, C. Wei, Weak fault detection and health degradation monitoring using customized standard multiwavelets, Mechanical Systems and Signal Processing 94 (2017) 384–399.

[14] J. Meng, C. Yan, Z. Wang, T. Wen, G. Chen, L. Wu, Health condition identification of rolling element bearing based on gradient of features matrix and mddcs-mrsvd, IEEE Transactions on Instrumentation and Measurement 71 (2022) 1–13.

[15] C. Lu, J. Chen, R. Hong, Y. Feng, Y. Li, Degradation trend estimation of slewing bearing based on lssvm model, Mechanical Systems and Signal Processing 76 (2016) 353–366.

[16] M. Mazzoleni, K. Sarda, A. Acernese, L. Russo, L. Manfredi, L. Glielmo, C. Del Vecchio, A fuzzy logic-based approach for fault diagnosis and condition monitoring of industry 4.0 manufacturing processes, Engineering Applications of Artificial Intelligence 115 (2022) 105317.

[17] Q. Li, C. Yan, W. Wang, A. Babiker, L. Wu, Health indicator construction based on md-cumsum with multi-domain features selection for rolling element bearing fault diagnosis, Ieee Access 7 (2019) 138528–138540.

[18] B. Hou, D. Wang, Y. Wang, T. Yan, Z. Peng, K.-L. Tsui, Adaptive weighted signal preprocessing technique for machine health monitoring, IEEE Transactions on Instrumentation and Measurement 70 (2020) 1–11.

[19] A. Kumar, C. Parkash, G. Vashishtha, H. Tang, P. Kundu, J. Xiang, State-space modeling and novel entropy-based health indicator for dynamic degradation monitoring of rolling element bearing, Reliability Engineering & System Safety 221 (2022) 108356.

[20] R. Yao, H. Jiang, C. Yang, H. Zhu, C. Liu, An integrated framework via key-spectrum entropy and statistical properties for bearing dynamic health monitoring and performance degradation assessment, Mechanical Systems and Signal Processing 187 (2023) 109955.

[21] A. Rai, J.-M. Kim, A novel health indicator based on information theory features for assessing rotating machinery performance degradation, IEEE Transactions on Instrumentation and Measurement 69 (2020) 6982–6994.

[22] H. Wang, X. Zhang, X. Guo, T. Lin, L. Song, Remaining useful life prediction of bearings based on multiple-feature fusion health indicator and weighted temporal convolution network, Measurement Science and Technology 33 (2022) 104003.

[23] L. Guo, Y. Lei, N. Li, T. Yan, N. Li, Machinery health indicator construction based on convolutional neural networks considering trend burr, Neurocomputing 292 (2018) 142–150.

[24] D. She, M. Jia, Wear indicator construction of rolling bearings based on multi-channel deep convolutional neural network with exponentially decaying learning rate, Measurement 135 (2019) 368–375.

[25] L. Chen, G. Xu, S. Zhang, W. Yan, Q. Wu, Health indicator construction of machinery based on end-to-end trainable convolution recurrent neural networks, Journal of Manufacturing Systems 54 (2020) 1–11.

[26] D. Chen, Y. Qin, Y. Wang, J. Zhou, Health indicator construction by quadratic function-based deep convolutional auto-encoder and its application into bearing rul prediction, ISA transactions 114 (2021) 44–56.

[27] C. Jiang, X. Liu, Y. Liu, M. Xie, C. Liang, Q. Wang, A method for predicting the remaining life of rolling bearings based on multi-scale feature extraction and attention mechanism, Electronics 11 (2022) 3616.

[28] J. Zhuang, Y. Cao, Y. Ding, M. Jia, K. Feng, An autoregressive model-based degradation trend prognosis considering health indicators with multiscale attention information, Engineering Applications of Artificial Intelligence 131 (2024) 107868.

[29] Y. Yoo, J.-G. Baek, A novel image feature for the remaining useful lifetime prediction of bearings based on continuous wavelet transform and convolutional neural network, Applied Sciences 8 (2018) 1102.

[30] L. Ren, Y. Sun, H. Wang, L. Zhang, Prediction of bearing remaining useful life with deep convolution neural network, IEEE access 6 (2018) 13041–13049.

[31] X. Li, W. Zhang, Q. Ding, Deep learning-based remaining useful life estimation of bearings using multi-scale feature extraction, Reliability engineering & system safety 182 (2019) 208–218.

[32] L. Guo, N. Li, F. Jia, Y. Lei, J. Lin, A recurrent neural network based health indicator for remaining useful life prediction of bearings, Neurocomputing 240 (2017) 98–109.

[33] A. E. Milani, D. Zappalá, S. J. Watson, A hybrid convolutional autoencoder training algorithm for unsupervised bearing health indicator construction, Engineering Applications of Artificial Intelligence 139 (2025) 109477.

[34] Z. Yang, P. Baraldi, E. Zio, A method for fault detection in multi-component systems based on sparse autoencoder-based deep neural networks, Reliability Engineering & System Safety 220 (2022) 108278.

[35] J. Zhou, Y. Qin, D. Chen, F. Liu, Q. Qian, Remaining useful life prediction of bearings by a new reinforced memory gru network, Advanced Engineering Informatics 53 (2022) 101682.

[36] A. Rai, S. H. Upadhyay, An integrated approach to bearing prognostics based on eemd-multi feature extraction, gaussian mixture models and jensen-rényi divergence, Applied Soft Computing 71 (2018) 36–50.

[37] L. Wen, G. Yang, L. Hu, C. Yang, K. Feng, A new unsupervised health index estimation method for bearings early fault detection based on gaussian mixture model, Engineering Applications of Artificial Intelligence 128 (2024) 107562.

[38] L. Fu, K. Yan, Y. Zhang, R. Chen, Z. Ma, F. Xu, T. Zhu, Edgecog: a real-time bearing fault diagnosis system based on lightweight edge computing, IEEE Transactions on Instrumentation and Measurement (2023).

[39] C. Pan, Y. Cao, Y. Yan, R. Shao, Review of recent patents on smart bearing, Recent Patents on Engineering 18 (2024) 13–39.

[40] Y. Gong, S. Wang, Z. Xie, T. Zhang, Z. Chen, W. Lin, W. Huang, A variable reluctance based rotational electromagnetic harvester for the high-speed smart bearing, Smart Materials and Structures 31 (2022) 045023.

[41] Y. Zhang, W. Wang, X. Wu, Y. Lei, J. Cao, C. Bowen, S. Bader, B. Yang, A comprehensive review on self-powered smart bearings, Renewable and Sustainable Energy Reviews 183 (2023) 113446.

[42] Y. Cui, P. Gao, W. Tang, G. Mo, J. Yin, Adaptive thin film temperature sensor for bearing's rolling elements temperature measurement, Sensors 22 (2022) 2838.

[43] L. Gong, Z. Zhang, R. Luan, Y. Feng, M. Gao, C. Zhang, Self-powered technologies for smart bearings, Fundamental Research (2025).

[44] L. Liu, X. Guo, W. Liu, C. Lee, Recent progress in the energy harvesting technology—from self-powered sensors to self-sustained iot, and new applications, Nanomaterials 11 (2021) 2975.

[45] M. Shirvanimoghaddam, K. Shirvanimoghaddam, M. M. Abolhasani, M. Farhangi, V. Z. Barsari, H. Liu, M. Dohler, M. Naebe, Towards a green and self-powered internet of things using piezoelectric energy harvesting, Ieee Access 7 (2019) 94533–94556.

[46] V. Sharma, U. Mukherji, V. Joseph, S. Gupta, Optimal energy management policies for energy harvesting sensor nodes, IEEE Transactions on Wireless Communications 9 (2010) 1326–1336.

[47] K. Das, P. Zand, P. Havinga, Industrial wireless monitoring with energy-harvesting devices, IEEE internet computing 21 (2017) 12–20.

[48] R. Tanash, M. AlQudah, S. Al-Agtash, et al., Enhancing energy efficiency of ieee 802.15. 4-based industrial wireless sensor networks, Journal of Industrial Information Integration 33 (2023) 100460.

[49] Y. Chu, P. Mitchell, D. Grace, J. Roberts, D. White, T. Mickus, Iris: A low duty cycle cross-layer protocol for long-range wireless sensor networks with low power budget, Computer Networks 225 (2023) 109666.

[50] S. Mulleti, T. Zirtiloglu, A. Tan, R. T. Yazicigil, Y. C. Eldar, Power-efficient sampling, arXiv preprint arXiv:2312.10966 (2023).

[51] G. Qian, S. Lu, D. Pan, H. Tang, Y. Liu, Q. Wang, Edge computing: A promising framework for real-time fault diagnosis and dynamic control of rotating machines using multi-sensor data, IEEE Sensors Journal 19 (2019) 4211–4220.

[52] D. Ma, G. Lan, W. Xu, M. Hassan, W. Hu, Simultaneous energy harvesting and gait recognition using piezoelectric energy harvester, IEEE Transactions on Mobile Computing 21 (2020) 2198–2209.

[53] F. Zangeneh-Nejad, D. L. Sounas, A. Alù, R. Fleury, Analogue computing with metamaterials, Nature Reviews Materials 6 (2021) 207–225.

[54] P. Peralta, R. Ruiz, S. Natarajan, E. Atroshchenko, Parametric study and shape optimization of piezoelectric energy harvesters by isogeometric analysis and kriging metamodeling, Journal of Sound and Vibration 484 (2020) 115521.

[55] P. Peralta-Braz, M. M. Alamdari, R. O. Ruiz, E. Atroshchenko, M. Hassan, Design optimisation of piezoelectric energy harvesters for bridge infrastructure, Mechanical Systems and Signal Processing 205 (2023) 110823.

[56] H. Qiu, J. Lee, J. Lin, G. Yu, Wavelet filter-based weak signature detection method and its application on rolling element bearing prognostics, Journal of sound and vibration 289 (2006) 1066–1090.

[57] K. Noman, U. Ali, Y. Li, S. Wang, A. U. Patwari, A. Kumar, A novel nonlinear dynamic measure for early detection of bearing fault using weighted squared envelope based symbolic lempel-ziv complexity, IEEE Transactions on Instrumentation and Measurement (2024).

[58] W. Zhu, G. Ni, Y. Cao, H. Wang, Research on a rolling bearing health monitoring algorithm oriented to industrial big data, Measurement 185 (2021) 110044.

[59] S. Schmidt, P. S. Heyns, K. C. Gryllias, A discrepancy analysis methodology for rolling element bearing diagnostics under variable speed conditions, Mechanical Systems and Signal Processing 116 (2019) 40–61.

[60] C. Liu, K. Gryllias, A semi-supervised support vector data description-based fault detection method for rolling element bearings based on cyclic spectral analysis, Mechanical Systems and Signal Processing 140 (2020) 106682.

[61] R. Hasani, G. Wang, R. Grosu, A machine learning suite for machine components' health-monitoring, in: Proceedings of the AAAI Conference on Artificial Intelligence, volume 33, pp. 9472–9477.

[62] C. Yi, S. Li, T. Huang, H. Xiao, Y. Jiang, On a prediction method for remaining useful life of rolling bearings via vmd-based dispersion entropy and gan, IEEE Sensors Journal (2023).

[63] H. Shi, L. Guo, S. Tan, X. Bai, Rolling bearing initial fault detection using long short-term memory recurrent network, IEEE Access 7 (2019) 171559–171569.

[64] S. Fong, S. Narasimhan, An unsupervised bayesian oc-svm approach for early degradation detection, thresholding, and fault prediction in machinery monitoring, IEEE Transactions on Instrumentation and Measurement 71 (2021) 1–11.

[65] H. Shi, J. Guo, X. Bai, L. Guo, Z. Liu, J. Sun, Research on a nonlinear dynamic incipient fault detection method for rolling bearings, Applied Sciences 10 (2020) 2443.

[66] W. Lu, Y. Li, Y. Cheng, D. Meng, B. Liang, P. Zhou, Early fault detection approach with deep architectures, IEEE Transactions on instrumentation and measurement 67 (2018) 1679–1689.

[67] Q. Wang, X. Liu, B. Wei, W. Chen, Online incipient fault detection method based on improved 1 trend filtering and support vector data description, IEEE Access 9 (2021) 30043–30059.

[68] S. Kass, A. Raad, J. Antoni, Self-running bearing diagnosis based on scalar indicator using fast order frequency spectral coherence, Measurement 138 (2019) 467–484.

[69] D. Wang, K.-L. Tsui, Q. Miao, Prognostics and health management: A review of vibration based bearing and gear health indicators, Ieee Access 6 (2017) 665–676.

[70] M. Yan, X. Wang, B. Wang, M. Chang, I. Muhammad, Bearing remaining useful life prediction using support vector machine and hybrid degradation tracking model, ISA transactions 98 (2020) 471–482.